ASCE

Improving the Ductility of Concrete Beams Reinforced with Topologically Optimized Steel

Yi Shao[1]; Tuo Zhao[2]; Jiayu Yan[3]; Claudia P. Ostertag[4]; and Glaucio H. Paulino[5]

Abstract: To address the sustainability challenges faced by concrete structures, various attempts have been made to optimize the reinforcement layout with a topologically optimized strut-and-tie model (STM). However, most studies have focused on theoretical discussions and the few available experimental studies have only discussed the prepeak behavior of optimized beams. The postpeak behavior, especially the ductility of beams with optimized reinforcement, has not been addressed, although it is one critical criterion for ensuring structural safety. Moreover, current topology optimization methods mostly adopt linear elastic material constitutive behavior, which neglects the intrinsic strength difference between steel and concrete material and has been found to cause low ductility in concrete beams. To address these challenges and enhance ductility with optimized reinforcement, this study proposes new frameworks for designing concrete beams with optimized reinforcement. The first framework enhances the elastic-material model-based optimized reinforcement layout with a postprocessing scheme to enhance concrete compression strut ductility. The second framework develops a new optimization formulation by introducing an asymptotic nonlinear material model, which considers both the stiffness and strength difference between concrete and steel material. An experimental and numerical program was conducted to compare the structural performance of concrete beams with optimized reinforcement from different frameworks. Results show that the new frameworks have limited impact on the peak strength but increase ductility of the optimized beams. Compared with the design from the conventional bilinear model, the design from the nonlinear model reduces steel consumption by 8.2%. **DOI: 10.1061/JSENDH.STENG-13908.** © *2025 American Society of Civil Engineers.*

Author keywords: Topology optimization; Nonlinear constitutive model; Ultrahigh-performance concrete (UHPC); Beam; Ductility.

Introduction

Concrete is the most consumed construction material in the world. To compensate for the low tensile capacity of concrete material, structural concrete members typically include steel cages with bars in both longitudinal and transverse directions. In this typical cage design, steel bars are usually not placed in the most effective paths for resisting the expected tensile forces under target loading and supporting conditions. Therefore, this design often consumes more steel material than the necessary amount, which increases self-weight and accelerates depletion of natural materials and emission of global warming gases.

For both animals and plants, the billions of years of evolution have generated optimized designs (e.g., bone structure) where materials are placed only in essential locations. In recent decades, numerical topology optimization methods have been developed to reproduce evolution and optimization in a short time. Topology optimization has been successfully applied in the aerospace and automotive industries to minimize material usage in metallic structures (Aage et al. 2017; Yang and Chahande 1995; Zhu et al. 2016). A few studies have developed topology optimization tools to optimize the reinforcement layout in concrete structures (Gaynor et al. 2013; Jewett and Carstensen 2019; Liang et al. 2002; Xia et al. 2020; Zegard and Paulino 2013). They are mostly focused on theoretical discussions, while experimental tests are rare. Jewett and Carstensen (2019) tested concrete beams with reinforcement layouts optimized by a hybrid bilinear approach. Relative to a standard strut-and-tie layout, their optimized layout improved structural efficiency but was not able to achieve high structural ductility, which is required in structural components.

This study is intended to develop a topology optimization–based reinforcement design framework that leads to ductile beam behavior. We first review current practice and challenges related to optimizing reinforcement layouts. We then propose two design frameworks: (1) one that combines classical bilinear optimization with a postprocessing tool; and (2) one that develops a new nonlinear optimization method. Experimental and numerical investigations are pursued to explore the performance of concrete beams designed based on these two frameworks.

Background

The strut-and-tie model (STM) is a simple and powerful tool for designing and analyzing structural concrete elements especially in the cracked states. After cracking, a concrete element can be

[1]Assistant Professor, Dept. of Civil Engineering, McGill Univ., Montreal, QC, Canada H3A0C3; Postdoctoral Scholar, Dept. of Civil and Environmental Engineering, Univ. of California, Berkeley, Berkeley, CA 94720 (corresponding author). ORCID: https://orcid.org/0000-0001-9722-9220. Email: yi.shao2@mcgill.ca

[2]Postdoctoral Scholar, Dept. of Civil and Environmental Engineering, Princeton Univ., Princeton, NJ 08540. ORCID: https://orcid.org/0000-0001-6004-8602. Email: tuo.zhao@princeton.edu

[3]Graduate Research Assistant, Dept. of Civil Engineering, McGill Univ., Montreal, QC, Canada H3A0C3. Email: jiayu.yan2@mail.mcgill.ca

[4]Professor, Dept. of Civil and Environmental Engineering, Univ. of California, Berkeley, Berkeley, CA 94720. ORCID: https://orcid.org/0000-0002-6182-3073. Email: ostertag@ce.berkeley.edu

[5]Professor, Dept. of Civil and Environmental Engineering, Princeton Univ., Princeton, NJ 08540; Professor, Princeton Materials Institute, Princeton Univ., Princeton, NJ 08540. Email: gpaulino@princeton.edu

Note. This manuscript was submitted on April 3, 2024; approved on October 8, 2024; published online on January 28, 2025. Discussion period open until June 28, 2025; separate discussions must be submitted for individual papers. This paper is part of the ***Journal of Structural Engineering***, © ASCE, ISSN 0733-9445.

idealized as a truss (Fig. 1) where tension force is carried by steel reinforcement (i.e., tension ties) and compression force is sustained by uncracked concrete pieces (i.e., compression struts). STM is typically used to predict the strength capacity of a concrete structure, where both concrete struts and steel ties are treated as linear-elastic members, which means only limited plastic deformation is allowed in concrete struts and steel ties should not yield (e.g., Schlaich et al. 1987; Williams et al. 2012). This limit of plasticity leads to a conservative estimation of the structure's actual load capacity according to the lower bound theory of plasticity (e.g., Schlaich et al. 1987; Williams et al. 2012). In other words, material nonlinearity (or plastic deformation) is expected to cause higher material stress and stress redistribution, resulting in higher load or deformation capacity (e.g., Hsu 1988; Zhou et al. 2018).

When designing a concrete member using the STM method, one of the most important steps is choosing an appropriate strut-and-tie layout (i.e., truss layout) since different truss layouts can be used for the same structural configuration, resulting in different levels of efficiency and safety (Schlaich et al. 1987; Williams et al. 2012). Schlaich et al. (1987) recommended a truss layout based on elastic stress distribution, which estimates the initial load paths but still relies on the engineers' experiences and judgment in choosing the layout. To automate and standardize the development of the truss layout, researchers have explored the possibilities of using topology optimization techniques.

STM truss layout has been optimized based on truss optimization [i.e., the ground structure method (Ali and White 2000, 2001; Bontempi and Malerba 2001)], continuum optimization (Almeida et al. 2013; Bruggi 2009, 2016; Herranz et al. 2012; Kwak and Noh 2006; Leu et al. 2006; Liang et al. 2002; Victoria et al. 2011; Xia et al. 2020; Zhiyi et al. 2018), or a combination of truss and continuum optimization (Amir and Sigmund 2013; Gaynor et al. 2013; Zegard and Paulino 2013). When continuum optimization is relied on, engineers still need to estimate the truss topology and determine the internal forces. Therefore, the ground structure method is naturally advantageous when optimizing the STM layout. These optimization schemes mostly adopt a single linear elastic material, while several studies have attempted to improve the material model by adopting a bilinear relationship (i.e., different modulus under tension and compression) to simulate steel in tension and concrete in compression (e.g., Gaynor et al. 2013). These methods, however, do not consider the strength differences between concrete and steel.

When designing concrete members using the classical STM method, two main types of steel reinforcement need to be designed. The first type is steel reinforcement in the tension ties, which carries the tension force across major cracks. Once a truss layout and the associated member forces are determined, positioning and proportioning the reinforcement is relatively easy and straightforward. The second type is the transverse reinforcement in the compression struts, which prevents abrupt splitting failure. In a concrete strut, compressive stress disperses from the small node zone when they flow through the struts, resulting in a bottle-shaped stress distribution [Fig. 1(b)]. When the compressive stresses change direction, transverse stresses develop to counteract the lateral components of the inclined compression stresses, causing axial splitting crack when the transverse tensile force exceeds the concrete cracking strength. This stress field can also be analyzed using a STM within the strut [Fig. 1(b)]. A Detailed description of this bottle-shaped stress distribution was first presented by Guyon (1953). Numerous studies have investigated the transverse reinforcement detailing in concrete struts (e.g., Brown and Bayrak 2006; Sahoo et al. 2011; Singh et al. 2018; Yuan et al. 2018), while different recommendations are made by design codes (e.g., CEN 2004; ACI 2019). In the few available studies that have explored the manufacturing of the

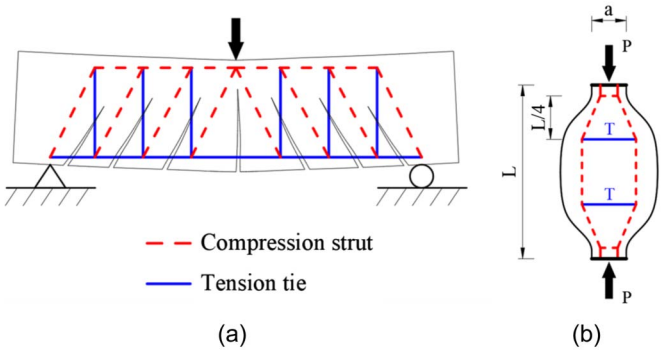

Fig. 1. Schematic of strut-and-tie model: (a) cracked beam; and (b) compression strut.

topology-optimized concrete structure in the literature, only the first type of steel was designed while the second was not (Jewett and Carstensen 2019; Liu et al. 2020). Therefore, the specimens mainly failed due to abrupt splitting failure along the strut axis (Jewett and Carstensen 2019; Liu et al. 2020). To achieve the best performance in the optimized specimens, the second type of reinforcement (i.e., in-strut transverse reinforcement) is included; it is described in the section "Design of Second Reinforcement Type."

Multimaterial Topology Optimization for STM

In this section, we propose a multimaterial topology optimization model to optimize STM layouts. Two material models are considered: a bilinear model and an asymptotic nonlinear model. One challenge that arises when nonlinearities are included in the analysis is how to define the objective function for maximum loading capacity. Klarbring and Strömberg (2013) maximized the total stationary potential energy, which is equivalent to minimizing compliance for linear problems and maximizing strain energy for material nonlinear problems (Zhao et al. 2019, 2020). Further, the strain energy objective was adopted by Zhao et al. (2023) for optimization of STM with bilinear material behavior, and it is adopted in this work for optimal STM layout design considering nonlinear elastic materials.

Optimization formulation maximizes the structural strain energy of the system in equilibrium subjected to volume constraints. Maximizing structural strain energy is equivalent to maximizing the strength capacity of the system. The topology optimization problem is subjected to prescribed energy, which leads to robust convergence in solving state equations considering material nonlinearity. Moreover, the system-prescribed energy guarantees a target minimum deformation capacity.

The ground structure–based optimization formulation considers two candidate materials (strut and tie) together with multiple volume constraints

$$\begin{aligned} &\max_{\boldsymbol{x}_1,\boldsymbol{x}_2} J(\boldsymbol{x}_1,\boldsymbol{x}_2) = U(\boldsymbol{x}_1,\boldsymbol{x}_2,\boldsymbol{u}(\boldsymbol{x}_1,\boldsymbol{x}_2)) \\ &\text{s.t.} \sum_{i\in G^j} \boldsymbol{L}_i^T \boldsymbol{x}_i - V^j_{\max} \le 0, \quad j = 1, \ldots, n \\ &\text{with} \quad \begin{cases} \boldsymbol{F}_{\text{int}}(\boldsymbol{x}_1,\boldsymbol{x}_2,\boldsymbol{u}(\boldsymbol{x}_1,\boldsymbol{x}_2)) = \lambda(\boldsymbol{x}_1,\boldsymbol{x}_2,\boldsymbol{u}(\boldsymbol{x}_1,\boldsymbol{x}_2))\boldsymbol{f}_0 \\ \boldsymbol{f}_0^T \boldsymbol{u}(\boldsymbol{x}_1,\boldsymbol{x}_2) = 2C_0 \end{cases} \end{aligned} \tag{1}$$

where $\boldsymbol{x}_1$ and $\boldsymbol{x}_2$ = vectors of design variables (cross-sectional areas of truss members) for struts (concrete) and ties (reinforcement),

respectively, which can be constrained separately; objective function J = structural strain energy; and $\boldsymbol{u}$ = displacement vector (state variable) obtained by solving the nonlinear state equations. Eq. (1) considers a total of n independent volume constraints and denotes G^j as the set of material indexes for the jth volume constraint where $\boldsymbol{L}_i^T \boldsymbol{x}_i$ indicates the total volume associated with the design variable $\boldsymbol{x}_i$, with $\boldsymbol{L}_i$ being the length vector for the ith material, and $V_{\max}^j$ is the allowable volume for the jth volume constraint. The main feature of Eq. (1) is that it can efficiently handle a general setting of volume constraints (Sanders et al. 2018; Zhang et al. 2018). In particular, defining material subregions allows control of the locations/inclination/length scale of the ties according to practical design requirements, which are elaborated in Appendix II.

To robustly solve the nonlinear state equations in Eq. (1), we propose an energy control approach together with Newton's method and inexact line search where $\boldsymbol{F}_{\text{int}}$ is the internal force vector, λ is the reaction force factor, $\boldsymbol{f}_0$ is the vector of given external forces, and C_0 is the prescribed energy in the structural system. The proposed approach allows flexible material properties, meaning that the constitutive model can be linear or nonlinear.

Asymptotic Nonlinear Elastic Constitutive Model

We present a nonlinear elastic material model based on limit analysis (Chen and Han 2007; Zhao et al. 2019). The strain-stress relationship for tie members and strut members, respectively, are defined as follows:

$$\text{Tie: } \sigma_i = \begin{cases} a_{\text{tie}} \arctan(b_{\text{tie}} \varepsilon_i) & \text{if } \varepsilon_i \geq 0 \\ 0 & \text{otherwise} \end{cases} \tag{2}$$

$$\text{Strut: } \sigma_i = \begin{cases} a_{\text{strut}} \arctan(b_{\text{strut}} \varepsilon_i) & \text{if } \varepsilon_i \leq 0 \\ 0 & \text{otherwise} \end{cases} \tag{3}$$

where $a_{\text{tie}} = 2\sigma_{\text{tie}}/\pi$, $b_{\text{tie}} = E_{\text{tie}}\pi/(2\sigma_{\text{tie}})$, $a_{\text{strut}} = 2\sigma_{\text{strut}}/\pi$, and $b_{\text{strut}} = E_{\text{strut}}\pi/(2\sigma_{\text{strut}})$; σ_{tie} and σ_{strut} = stress limits of the tie members and strut members, respectively; E_{tie} is Young's modulus of tie members; and E_{strut} is Young's modulus of strut members. Based on the strain-stress relationship formulas in Eqs. (2) and (3), we can derive the explicit strain energy density functions as

$$\text{Tie } \Psi_i = \begin{cases} a_{\text{tie}} \varepsilon_i \arctan(b_{\text{tie}} \varepsilon_i) - \dfrac{a_{\text{tie}}}{2b_{\text{tie}}} \left[\ln\left(\dfrac{1}{b_{\text{tie}}^2} + \varepsilon_i^2\right) - \ln\left(\dfrac{1}{b_{\text{tie}}^2}\right) \right] & \text{if } \varepsilon_i \geq 0 \\ 0 & \text{otherwise} \end{cases} \tag{4}$$

$$\text{Strut } \Psi_i = \begin{cases} a_{\text{strut}} \varepsilon_i \arctan(b_{\text{strut}} \varepsilon_i) - \dfrac{a_{\text{strut}}}{2b_{\text{strut}}} \left[\ln\left(\dfrac{1}{b_{\text{strut}}^2} + \varepsilon_i^2\right) - \ln\left(\dfrac{1}{b_{\text{strut}}^2}\right) \right] & \text{if } \varepsilon_i \leq 0 \\ 0 & \text{otherwise} \end{cases} \tag{5}$$

Fig. 2(a) shows the stress–strain profiles of the present nonlinear model for tie members. The initial slope of the curve is defined by the material Young's modulus E_{tie}. As the strain increases, the stress asymptotically reaches a plateau defined by the stress limit σ_{tie}. The stress profile of strut members shown in Fig. 2(b) exhibits similar asymptotic behavior for given E_{strut} and σ_{strut}. The stress–strain curves show that the stress function is not differentiable at zero strain; however, the strain energy density function is continuous and differentiable as shown in Figs. 2(c and d).

Optimized STM Layouts

We demonstrate the design optimization results with a simply supported beam subject to four-point bending. These beams are considered D-region beams since the distance between the loading and support points is less than two times the effective depth (ACI 318-19), which are the target application structures for the STM method. Concrete beams with these designs are analyzed, fabricated, and tested subsequently.

Using the optimization formulation in Eq. (1), we investigate optimized STM layouts considering three material constitutive models: standard linear elastic, bilinear, and the presented asymptotic nonlinear elastic. The material parameters used in the numerical simulation are summarized in Table 1. We assume the total volume of strut members and tie members to be identical in the three case studies. In addition, we apply the same amount of input energy $C_0 = 2$ kJ. The selection of this C_0 value is explained in Appendix III.

Fig. 3(a) shows the linear optimization results. As expected, the stress profile shows that all strut and tie members have equal stress values but opposite signs. This design is ideal for materials that have equal stiffness and strength at compression and tension so the struts and ties can reach the maximum stress capacity at the same time, contradicting the strength differences between concrete and steel. Fig. 3(b) demonstrates the optimized STM layout considering bilinear material modeling. Notice that the geometrical complexity of the bilinear result has been greatly reduced compared with the linear result. Moreover, the stress profile verifies that the ratio between the strut member and the tie member satisfies the condition $\sigma_{\text{strut}}/\sigma_{\text{tie}} = \sqrt{E_{\text{strut}}/E_{\text{tie}}}$ (Achtziger 1996). While the tie (i.e., steel reinforcement) stress can be 2.2 times the strut (i.e., concrete) stress, this strength ratio is still lower than the actual ratio between steel tensile strength and concrete compressive strength (i.e., ratio = 3.3). This means that the concrete struts reach their compressive strength before the steel ties reach their tensile strength, which contradicting the typical reinforced concrete design philosophy where steel should reach tensile yield strength before the concrete crushes (i.e., reach the compressive strength). Therefore, relatively low structural ductility is expected. Lastly, Fig. 3(c) shows a representative nonlinear elastic solution. We observe from the stress profile that struts and tie members reach their strength limit simultaneously. This behavior is more ideal compared with linear and bilinear optimization results since it allows the steel

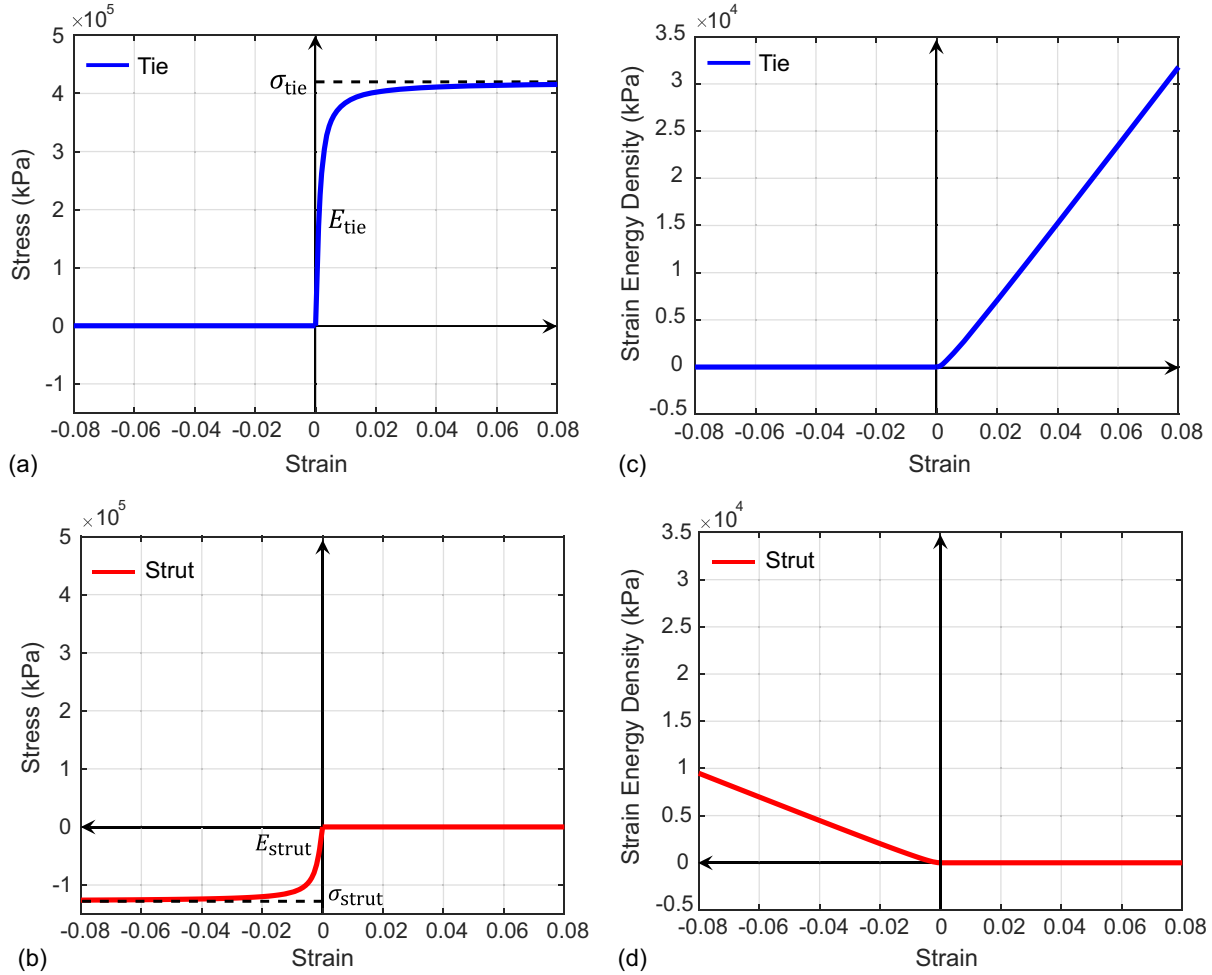

Fig. 2. Asymptotic nonlinear elastic constitutive material model: (a and b) strain–stress relationship, where E_{tie} and E_{strut} denote Young's modulus of tie members and strut members, respectively; σ_{tie} and σ_{strut} = stress limits of the tie members and strut members, respectively. (c and d) Strain energy density curves for tie members and strut members, respectively.

Table 1. Material properties used in design optimization of simply supported beam

Material modeling	Strut elastic modulus E_{strut} ($\times 10^3$ MPa)	Tie elastic modulus E_{tie} ($\times 10^3$ MPa)	Strut stress limit σ_{strut} (MPa)	Tie stress limit σ_{tie} (MPa)
Linear	41.6	41.6	NA	NA
Bilinear	41.6	200	NA	NA
Nonlinear	41.6	200	−128	420

to yield when concrete crushes, so we can use the high structural ductility provided by the steel yielding plateau, which is the typical structural behavior in properly designed reinforced concrete beams.

Design of Second Reinforcement Type

In this study, the second reinforcement type is designed according to the following procedure. The transverse reinforcement is most effective when placed at the regions with the highest lateral tensile stress (i.e., where a splitting crack initiates). According to Eurocode 2 (CEN 2004), the transverse reinforcement must be at a distance of approximately L/4 [L = strut length; Fig. 1(b)] from the node. Note that the amount of transverse reinforcement obtained from the suggested framework is considered conservative based on current knowledge. The transverse reinforcement must

- Meet minimum transverse reinforcing ratio for compression struts per ACI 318-19 (ACI 2019): $\rho_{t,\min,ACI} = 0.0025/\sin^2\alpha$, where α = angle between the transverse reinforcement and the strut axis;
- Meet minimum transverse reinforcing ratio to avoid abrupt failure after splitting crack initiation (Sahoo et al. 2011): $\rho_{t,\min,split} = 0.5 \cdot f_{cr}/(f_{t,sy} \cdot \sin^2\alpha)$, where f_{cr} = matrix cracking strength. $f_{t,sy}$ = transverse reinforcement yield strength.
- Balance the lateral force within the strut. For each inner tension truss, the lateral force is estimated per Eurocode 2 (CEN 2004) as: $T = 0.25 \cdot (1 - 0.7 \cdot a/L) \cdot P$, with dimensions and forces shown in Fig. 1(b). Therefore, the steel area for each inner tension truss shall be greater than: $A_{t,\min,\ tension} = T/f_{t,sy}$.

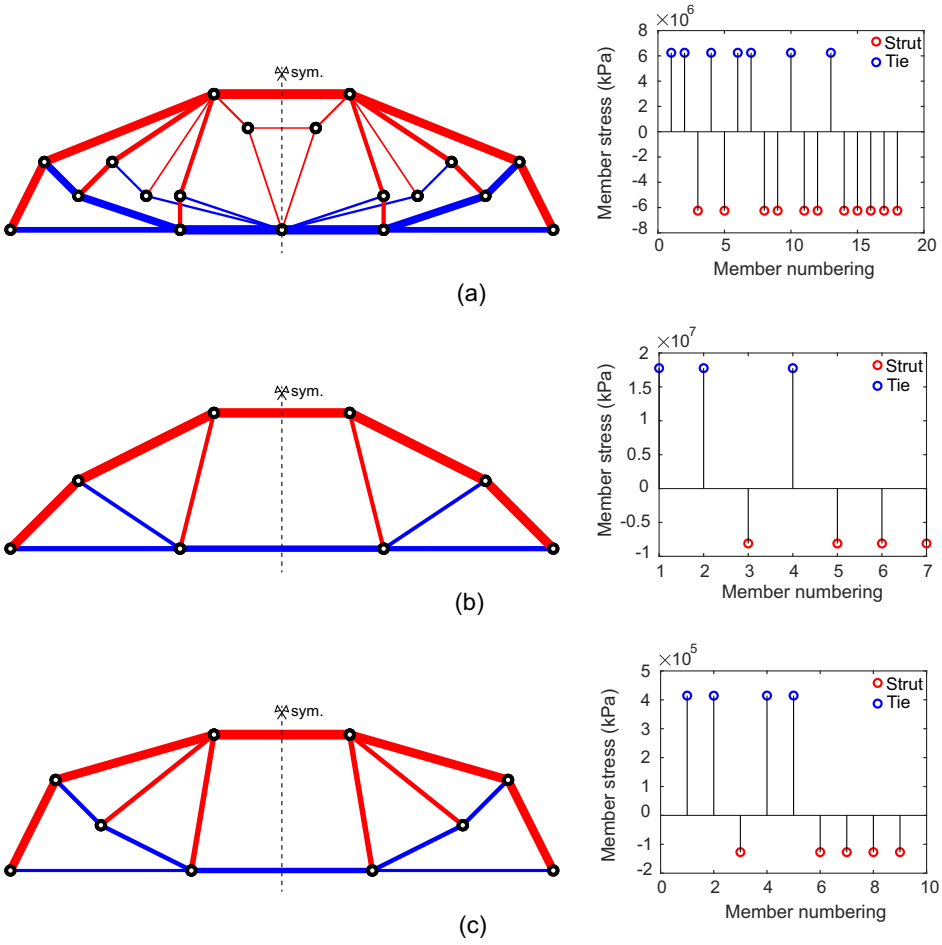

Fig. 3. Optimized STM layouts: (a) linear elastic material constitutive model; (b) bilinear material model; and (c) asymptotic nonlinear elastic model. Inset plots are stress profiles for each layout. Red and blue circles represent the stress states of strut members and tie members, respectively. The geometry of the optimized layouts is symmetrical, so the stress profiles include stress states for only half of the total members.

Experimental and Numerical Program

In this section, the behavior of beams with different reinforcement layouts is studied using experimental tests and numerical simulation. The numerical simulation is intended to enhance the understanding of the experimental results. The reinforcement layouts are based on the bilinear and nonlinear optimization results. Linear optimization results are not included for validation, as they neglect both the stiffness and strength differences between concrete and steel materials and are not appropriate for practical design (Gaynor et al. 2013; Du et al. 2019).

Materials

We adopted an ultrahigh performance concrete (UHPC) as the matrix material. This UHPC is a non-proprietary material developed at University of California, Berkeley (Aghdasi and Ostertag 2018). To enhance the material toughness, 1% by volume of steel fibers are added to this UHPC matrix. These steel fibers had a diameter and length of 0.2 mm and 13 mm, respectively. After casting, the specimens were moisture cured until three days before a test age of around 35 days. Uniaxial compression tests were applied to three 50 mm cubes, and the average compressive strength was determined to be 135.3 MPa.

The steel reinforcement was A871 Gr65 steel plates with 9.5 mm thickness. Uniaxial tension tests were performed on steel coupons with a cross-section size and gauge length of 9.5 mm × 9.5 mm and 50 mm. Fig. 4 shows the representative stress–strain curve of the adopted steel. The yielding and ultimate strength of the reinforcing steel were 515 MPa and 673 MPa, respectively.

Beam Design and Loading

Fig. 5 presents the beam reinforcement design. A tension reinforcing ratio of 3.7% was chosen to fully utilize the high compressive

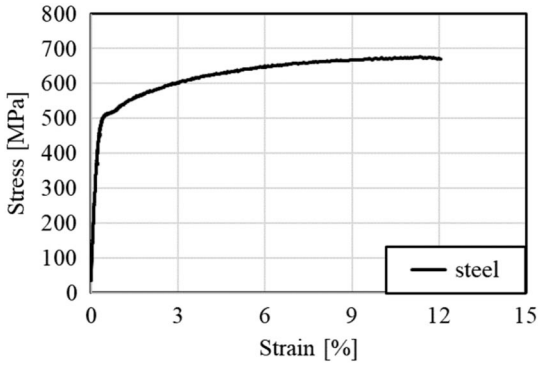

Fig. 4. Stress–strain curve of the adopted steel.

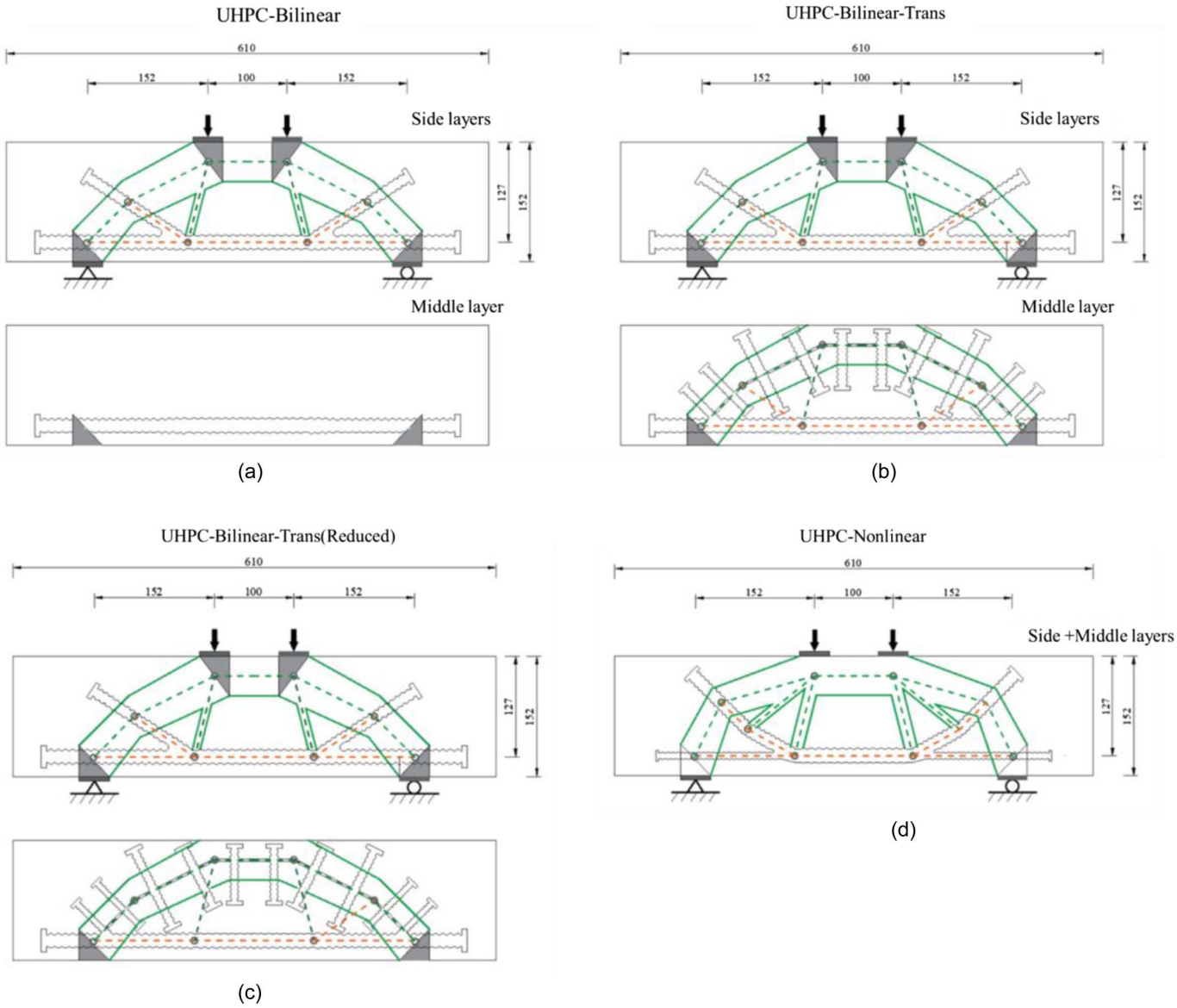

Fig. 5. Reinforcement design: (a) optimized reinforcement based on bilinear results; (b) optimized reinforcement based on bilinear results, with additional transverse steel for struts; (c) optimized reinforcement based on bilinear results and with additional transverse steel for struts—transverse steel width reduced from (b) considering UHPC tensile strength; and (d) optimized reinforcement based on nonlinear results.

strength and high crushing resistance of UHPC material. Based on the expected tension force in the midspan bottom tension tie, the expected compression forces in struts and tension forces in ties can be estimated based on force ratios from the optimization results (Fig. 3). The compression strut width is estimated using $C/(f_{ce} \times t_b)$, where C = estimated compression force; f_{ce} = effective compressive strength; and t_b = beam thickness. According to ACI 318-19, for a compressive strut with transverse reinforcement, f_{ce} can be conservatively estimated as $f_{ce} = 0.63 \times f'_c$. Similarly, the tension tie width is estimated using $T/(f_s \times t_s)$, where T = estimated tension force; f_s = steel strength; t_s = steel plate thickness. Steel yielding strength is adopted for all tension ties and second transverse reinforcement type except the longitudinal tension tie at midspan (i.e., between the two nodes near the bottom center). For this midspan longitudinal tension tie, the ultimate tensile strength is assumed because at the ultimate stage (crushing point), longitudinal steel at midspan has been observed to reach ultimate strength in UHPC beam tests (Shao and Billington 2022).

A total of four beams are designed. The reinforcement of each beam is made of three parallel layers of steel reinforcement, which is composed of two identical side layers and one middle layer (Fig. 5). Fig. 6 is a three-dimensional rendering of the reinforcement design of UHPC-Bilinear. UHPC-Bilinear is designed based purely on the bilinear optimization result [Fig. 3(b)]. The required longitudinal tension reinforcement at the bottom is equally divided by the three reinforcement layers while the inclined reinforcement is equally divided by the two side layers. For UHPC-Bilinear-Trans, the second transverse reinforcement type is added to the middle layer based on the design method outlined in section "Background." The splitting resistance from UHPC fiber-bridging is neglected in the beam design. For UHPC-Bilinear-Trans (Reduced), the needed tension force from the second reinforcement type is estimated as $T = 0.25 \times (1 - 0.7 \times a/L) \times P - L \cdot b \cdot f_t/2$, where f_t is the estimated UHPC tensile strength. The first part represents the estimated lateral force based on Eurocode (CEN 2004), while the second part represents the estimated splitting resistance provided by fiber-bridging. UHPC tensile strength (f_t) is estimated

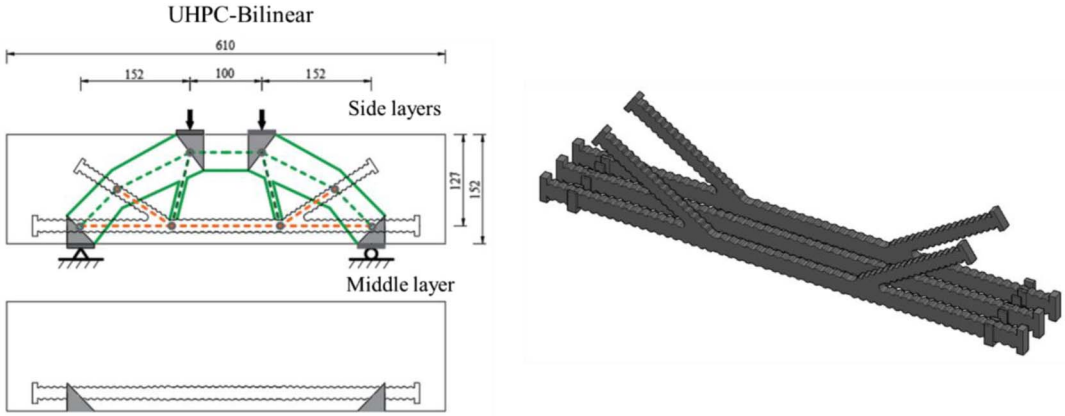

Fig. 6. Three-dimensional rendering of reinforcement layout for UHPC-Bilinear.

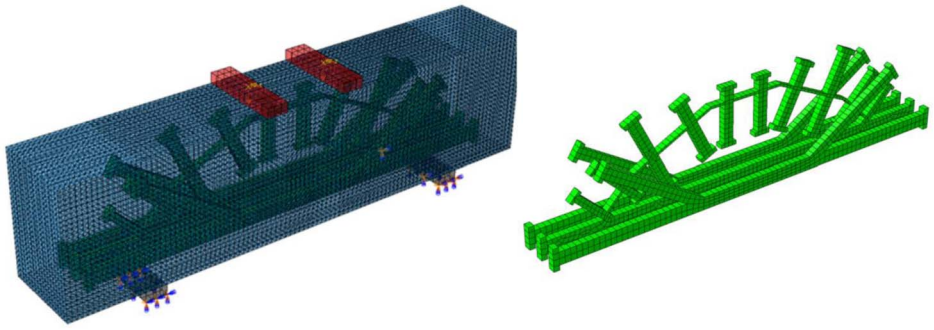

Fig. 7. Numerical model of UHPC-Bilinear-Trans.

as 5-MPa based on Shao and Ostertag (2023), who adopted the same material. To be conservative in estimating UHPC splitting resistance, a 50% strength reduction factor is applied to UHPC tensile strength to consider the randomness of fiber distribution and the possible occurrence of unfavorable fiber distribution (Duque and Graybeal 2017). For beam UHPC-nonlinear, the tension reinforcement is designed based on the optimization result [Fig. 3(c)] and equally divided by three layers. No second transverse reinforcement type is added. The design of the rib is described in Appendix I.

For each beam design, two identical beams were fabricated and tested in the CEE Structures Lab at UC Berkeley to verify repeatability. The beams are simply supported and subject to four-point bending (Fig. 5) at a quasi-static loading rate of approximately 0.02 mm/s. The applied load is recorded by the load cell in the universal test machine, while the midspan deflection is recorded by linear variable differential transformer (LVDT).

Numerical Modeling

The numerical simulations were performed based on Abaqus/Explicit. Finite-element (FE) models were built with simplified steel reinforcements at full scale, as shown in Fig. 7. Due to the complexity of the matrix geometry, UHPC parts were meshed using C3D10M elements with an approximate globe size of 6 mm, while reinforcements parts were meshed using C3D8R elements with an approximate globe size of 5–9 mm for different FE models. Reinforcements embedded in the UHPC region in the FE models and displacement-controlled loads of 25 mm were applied.

Constitutive Models

The constitutive relationship for steel reinforcements are described by a plasticity material model based on the results of uniaxial tension tests (Fig. 4). For the matrix, a fracture energy–based model proposed by Shao et al. (2021) was used to predict the behavior of the UHPC material. Tables 2 and 3 lists the material properties for the simulation. In ABAQUS, the concrete damaged plasticity (CDP) model option was adopted and concrete failure was set at 0.15 tensile strain to simulate crack development.

Results and Discussions

Fig. 8 compares the load-displacement responses of a representative beam of each design, while Fig. 9 presents the load-displacement responses of all experimental beams and numerical

Table 2. Material properties of steel reinforcement

Grade	Yield strength $f_{y,m}$ (MPa)	Ultimate tensile strength $f_{u,m}$ (MPa)	Yield strain ε_y (%)	Elastic modulus E ($\times 10^3$ MPa)	Elongation s (%)
A871 Gr65	515	673	0.56	206	27

Table 3. Material properties of UHPC

Concrete type	Tensile strength $f_{t,p}$ (MPa)	Compressive strength f'_c (MPa)	Tensile fracture energy G_f (MPa-mm)	Compressive fracture energy G_c (MPa-mm)	Tensile localization strain $\varepsilon_{t,p}$ (%)	Elastic modulus E ($\times 10^3$ MPa)
UHPC	4.3	135.5	4.9	185	0.01	43.7

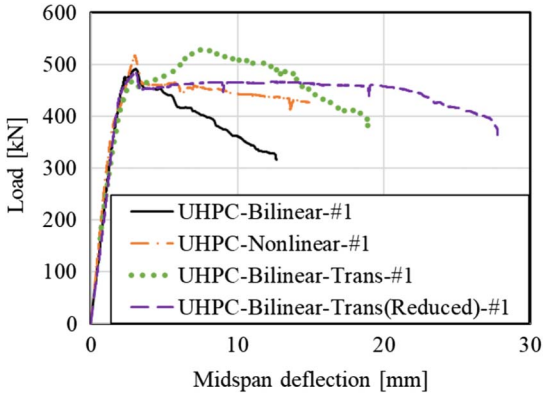

Fig. 8. Representative load-deflection responses.

simulation results to show repeatability. Fig. 10 compares the crack pattern of the representative beams, which is similar to the numerical crack pattern.

All beams behave nearly linearly until a load of around 350 kN, when hairline flexural or shear cracks start developing. At the first peak load (around 2.5-mm displacement and 470-kN load), transverse splitting cracks form along the top compression strut and compressive damage is visible [Fig. 10(a)]. For UHPC-Bilinear, the load capacity drops relatively quickly after the splitting crack initiates. This is expected since only fiber reinforcement is available to resist the splitting crack but it cannot provide the required splitting resistance.

After adding transverse reinforcement, UHPC-Bilinear-Trans reached a second, higher load-capacity peak since adequate splitting resistance is provided, which allows the compression strut to develop higher compression force. This is demonstrated by the

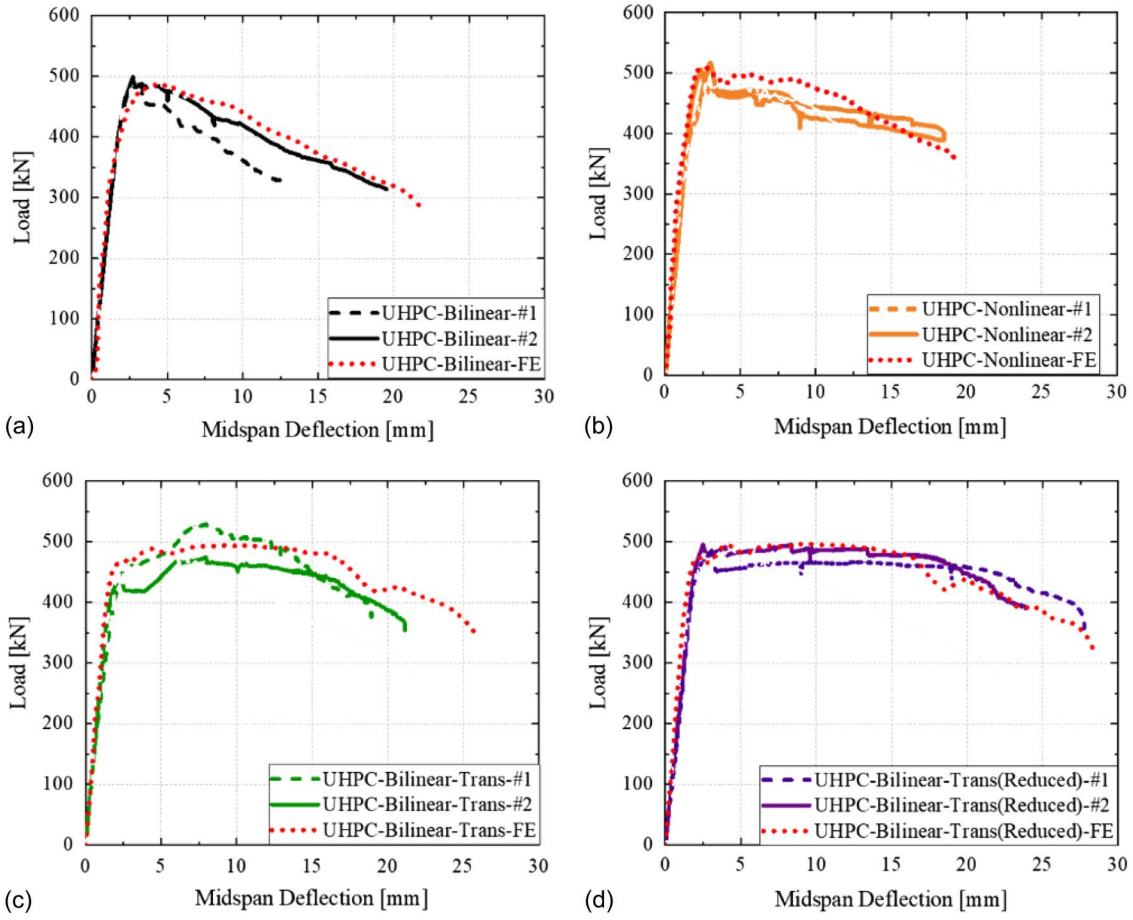

Fig. 9. Load-deflection responses for both experimental and FE simulation results: (a) UHPC-Bilinear; (b) UHPC-Nonlinear; (c) UHPC-Bilinear-Trans; and (d) UHPC-Bilinear-Trans (Reduced).

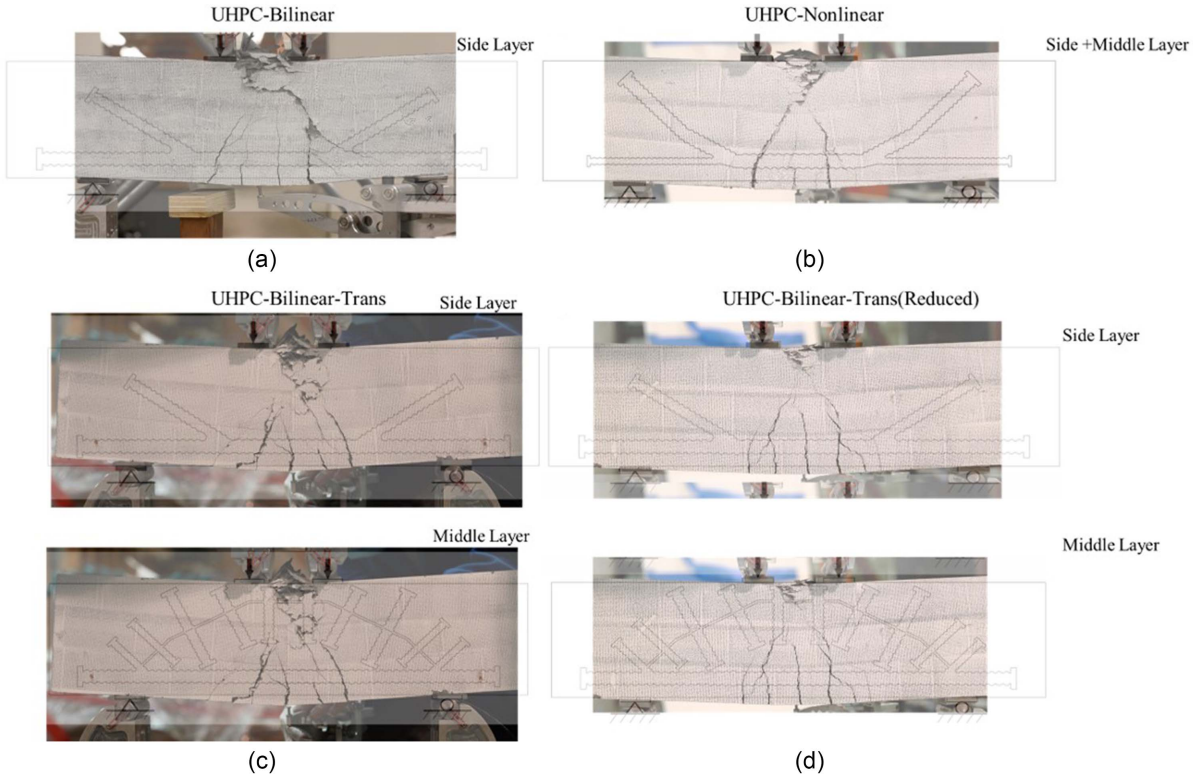

Fig. 10. Representative crack patterns: (a) UHPC-Bilinear; (b) UHPC-Nonlinear; (c) UHPC-Bilinear-Trans; and (d) UHPC-Bilinear-Trans (Reduced). Parts (c and d) show crack pattern against either middle or side layer.

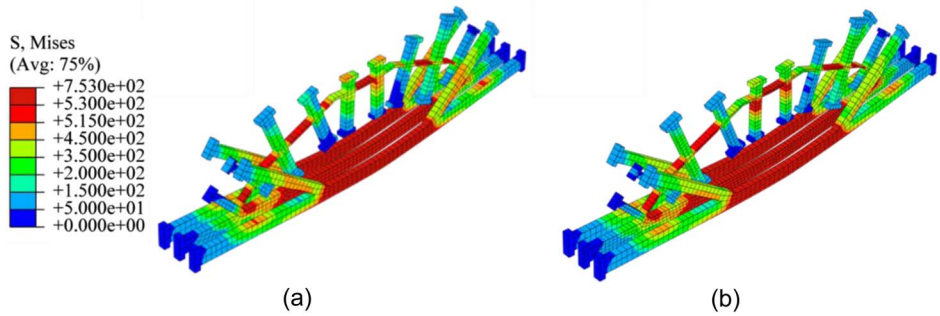

Fig. 11. Von Mises stress distribution of steel reinforcement: (a) UHPC Bilinear-Trans-FE; and (b) UHPC Bilinear-Trans (Reduced)-FE at peak load.

stress contour shown in Fig. 11(a). The transverse reinforcement along the top compression strut is heavily stressed, indicating that it resists the top compression strut splitting failure observed in UHPC-Bilinear. Even with reduced transverse reinforcement, UHPC-Bilinear-Trans (Reduced) maintains the load capacity and forms a load plateau. Comparing these two beams with transverse reinforcement, UHPC-Bilinear-Trans achieves higher load capacity but lower ductility, while UHPC-Trans (Reduced) exhibits a slightly lower load capacity but higher ductility. Additionally, the transverse steel along the top compression structure in UHPC-Bilinear-Trans (Reduced) [Fig. 11(b)] is more stressed than the counterparts in UHPC-Bilinear-Trans [Fig. 11(a)], demonstrating the effectiveness of reducing the transverse steel to enhance utilization efficiency.

UHPC-Nonlinear's load capacity reduces after reaching the first peak but at a slower rate. This could be attributed to the advantages of considering the strength limit of UHPC and steel material. Allowing steel to reach the yielding plateau when the compression strut softens leads to higher ductility. In other words, UHPC-Bilinear can be treated as an overreinforced beam where the compression strut fails before the steel yields, which is expected to exhibit low ductility. UHPC-Nonlinear transforms the beam to a balanced design by allowing the steel to yield when the compression strut fails, which improves ductility.

Steel Consumption

Table 4 compares steel consumption by the four designs. Compared with UHPC-Bilinear, the two designs with secondary reinforcement increases steel consumption 27.3% and 32.6%. While these two designs [UHPC-Bilinear-Trans and UHPC-Bilinear-Trans (Reduced)] effectively enhance the ductility of UHPC-Bilinear, this

Table 4. Steel consumption

Name	Steel consumption (cm^3)	Relative change to UHPC-Bilinear (%)
UHPC-Bilinear	334	—
UHPC-Bilinear-Trans	443	32.6
UHPC-Bilinear-Trans (Reduced)	426	27.3
UHPC-Nonlinear	307	−8.2

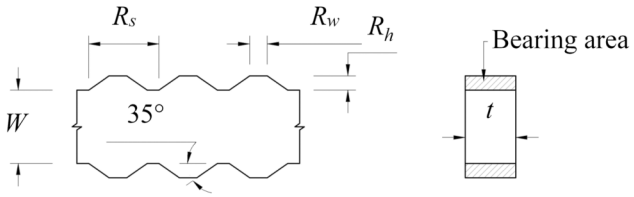

Fig. 12. Rib design.

27.3%–32.6% increase in steel consumption could significantly increase costs and enlarge carbon footprints. On the other hand, UHPC-Nonlinear reduces the steel consumption of UHPC-Bilinear by 8.2% while increasing postpeak ductility. Therefore, the nonlinear optimization algorithm can be considered an ideal choice for enhancing ductility without increasing material consumption.

Conclusions

This study aimed at improving the structural ductility of concrete beams with topologically optimized reinforcement layouts. Existing bilinear optimization is found to cause low structural ductility First, it only considers the stiffness difference between concrete and steel, so concrete struts reach their compressive strength before steel ties reach their tensile strength, which results in an overreinforced design and low structural ductility. Second, transverse reinforcement, which is necessary for enhancing the ductility of compression ties, is not considered. This study proposes two new design frameworks to address these two challenges.

In the first framework, a postprocessing step is added to the bilinear optimization results to provide the compression struts with transverse reinforcement. Transverse reinforcement effectively resists splitting failure along compression struts, which causes failure in pure bilinear optimization–based beams. With the transverse reinforcement, the new beam designs achieve a second, and higher, peak load after the splitting crack forms, which enhances the structural ductility of the beam design.

In the second framework, the authors propose a nonlinear topology optimization method that considers the stiffness and strength difference between the concrete and steel materials, which allows the concrete struts and steel ties to reach their desired strength simultaneously. This means that the beam changes from an overreinforced design to an under-reinforced design. Therefore, the nonlinear solution shows a more gradual load decline than the bilinear solution and enhances structural ductility.

While these two frameworks are effective in enhancing the structural ductility of bilinear beam designs, future studies may be needed to test the new frameworks on beams with different materials (e.g., conventional concrete, high-strength concrete) and geometries.

Appendix I. Rib Design

Surface deformation in the form of ribs is important in generating bonding between steel reinforcement and the surrounding UHPC or concrete matrix, ensuring a composite behavior. The overarching goal of our rib design (Fig. 12) is to match the rib pattern of a common mild steel reinforcing bar in terms of the rib topology as well as the ratio between the bearing area (i.e., the cross-sectional area of the rib perpendicular to the bar axis, $2 \times R_h \times t$ in Fig. 12) and the tension-force carrying area ($W \times t$ in Fig. 12). To achieve this goal, the authors measured several steel bars (with diameters of 10–25 mm) in our lab with reference to ACI 408 (ACI 2003) and ASTM A615-16 (ASTM 2016). Once the width of the reinforcement, W, is determined based on the needed tension force, the equivalent round (i.e., circular) bar diameter, $d_{b,eq}$ can be calculated by the rule of the same tension-force carrying area: $d_{b,eq} = \sqrt{2} \times W \times t/\pi$. The rib spacing ($R_s$) and Rib width ($R_w$) are estimated to match those of an equivalent round bar: $R_s = 0.7 \times d_{b,eq}$ and $R_w = 0.25 \times R_s$. The needed bearing area for an equivalent round bar is estimated as $A_{\text{bearing}} = 0.06 \times \pi \times d_{b,eq} \times R_s$. Then the rib height can be calculated by $R_b = (A_{\text{bearing}}/2 \times t)$. This methodology generates a rib pattern that brings bonding force similar to circular bars with an equivalent diameter. During experiments, no noticeable slippage was observed between the steel reinforcement and the surrounding matrix. Other rib design methods engineered for water-jet cutting steel (e.g., Higuchi et al. 2022) may be adopted; they are not within the scope of this study.

Appendix II. Material Subregions

Defining the subregions of struts and ties plays a major role in designing optimized STM layouts. For the present numerical examples, the design domain is discretized by a 12×6 grid, and the standard symmetry boundary conditions are applied, as shown in Fig. 13(a). For optimization considering linear and bilinear materials modeling, the initial ground structures (GSs) for both the strut layer and the tie layers are identical—full-level GS connecting each and every node in the design domain.

We investigated three subregion assignments and their influence on STM layouts, using the asymptotic nonlinear material model. Our emphasis was on the control of tie inclinations and length scales. These are important from a practical point of view because the difficulties in constructing the deep beam highly depend on the design of ties in the STM. In the first design, both tie and strut layers have full-level GS; the optimized layout is shown in Fig. 13(b) with load factor $\lambda = 108.47$. The load factor defined in Eq. (1) indicates the loading capacity of the STM design.

In the second design, the strut layer has full-level GS, while the tie layer assumes the removal of members with an inclination angle of less than 25°, which is recommended by ACI 318-19 (ACI 2019). The corresponding solution is shown in Fig. 13(c), which has a less complex layout than the first design. The optimized layout can be further simplified by restricting the members in the initial GS for the ties. For example, assuming that the minimum member length is 3, the optimized design is obtained, as shown in Fig. 13(d). Comparing the three solutions, the latter two impose additional inclination and length scale constraints in the optimization problem. As expected, the load factors of layouts in the second and the third designs are lower than that of the result in the first design.

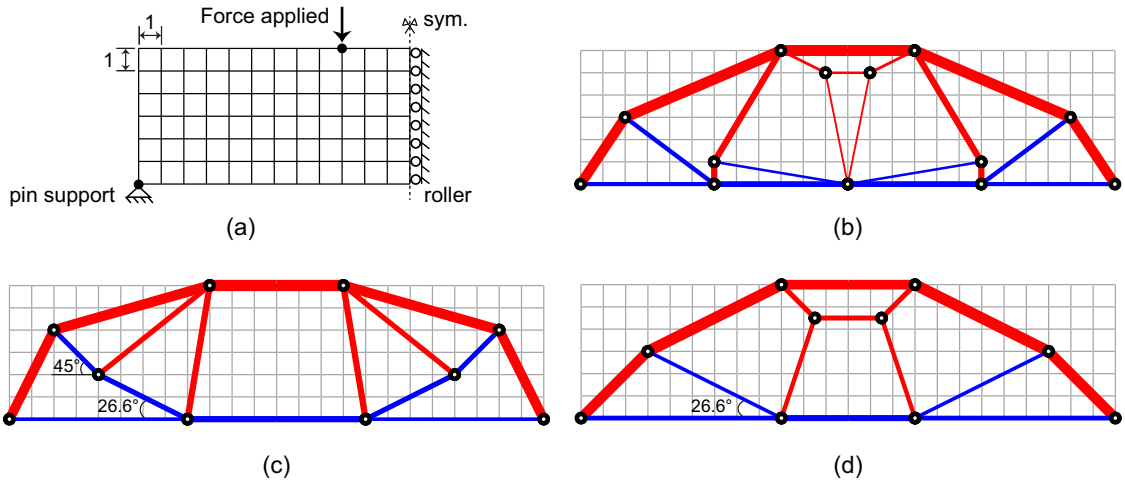

Fig. 13. Alternative nonlinear optimized STM layouts with flexible inclination/length controls: (a) design domain, boundary, and loading conditions; (b) optimized design without inclination or length constraints for both struts and ties; (c) optimized layout with inclination constraint for ties, where lower bound of allowable angle is 25°; and (d) optimized layout with both inclination and length constraints for ties, where lower bound of permissible angle is 25° and minimum length is 3.

Appendix III. Selection of Prescribed Energy C_0

The selection of C_0 depends on the expected nonlinear behavior of the optimized design. For the asymptotic nonlinear optimization scheme, choosing a value of C_0 is considered a way of controlling when both struts and ties reach the yielded stress limit. Here, we provide a rational approach to estimate the input value C_0 for the optimization problems considering the nonlinear material model. Given a design problem with specific boundary and loading conditions, we first generate a reference topology by standard linear materials modeling. Since linear materials optimization is insensitive to the input C_0, we arbitrarily select a value, 0.002 kJ, to obtain a linear optimized design, as shown in Fig. 14(a). The corresponding stress plot shows that both strut and tie members have constant stress values. Next, we conduct structural analysis considering asymptotic nonlinear modeling. For the input $C_0 = 0.002$ kJ, neither strut members nor tie members reach the given yield stress limits [Fig. 14(b)]. After we increase the input energy to 2 kJ, we observe that the stress on the struts reaches its prescribed yielding limit [Fig. 14(c)]. Thus, 2 kJ is selected as the input for nonlinear optimization. Finally, we obtained the nonlinear optimized design shown in Fig. 3(c).

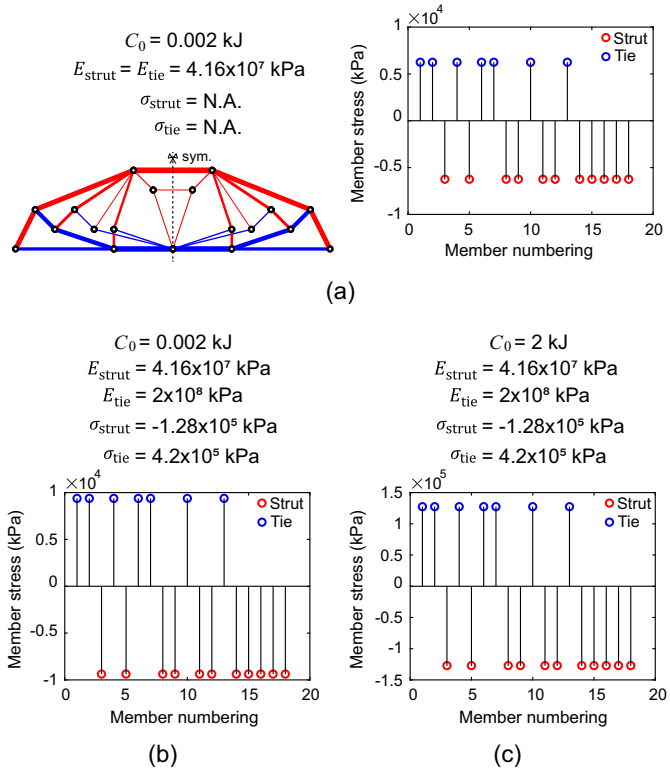

Fig. 14. Structural analysis of linear optimized design considering: (a) input $C_0 = 0.002$ kJ and standard linear elastic material modeling; (b) input $C_0 = 0.002$ kJ and asymptotic nonlinear material modeling; and (c) input $C_0 = 2$ kJ and asymptotic nonlinear material modeling.

Data Availability Statement

Some or all data, models, or code that support the findings of this study are available from the corresponding author upon reasonable request.

Acknowledgments

The authors appreciate the assistance of the lab staff at the Structures Lab at UC Berkeley, where the beam tests were carried out, and the support from UC Berkeley's Jacobs Institute for Design Innovation for the steel water-jet cutting service. We appreciate the lab assistance from Hannah Dam and Zane Schemmer. Authors Yi Shao and Tuo Zhao contributed equally to this work.

References

Aage, N., E. Andreassen, B. S. Lazarov, and O. Sigmund. 2017. "Giga-voxel computational morphogenesis for structural design." *Nature* 550 (7674): 84–86. https://doi.org/10.1038/nature23911.

Achtziger, W. 1996. "Truss topology optimization including bar properties different for tension and compression." *Struct. Optim.* 12 (1): 63–74. https://doi.org/10.1007/BF01270445.

ACI (American Concrete Institute). 2003. *Bond and development of straight reinforcing bars in tension (reapproved 2012)*. ACI PRC-408-03. Farmington Hills, MI: ACI.
ACI (American Concrete Institute). 2019. *Building code requirements for structural concrete*. ACI 318M-19. Farmington Hills, MI: ACI.
Aghdasi, P., and C. P. Ostertag. 2018. "Green ultra-high performance fiber-reinforced concrete (G-UHP-FRC)." *Constr. Build. Mater.* 190 (Nov): 246–254. https://doi.org/10.1016/j.conbuildmat.2018.09.111.
Ali, M., and R. White. 2000. "Formulation of optimal strut-and-tie models in design of reinforced concrete structures." *Spec. Publ.* 193 (Aug): 979–998. https://doi.org/10.14359/9971.
Ali, M. A., and R. N. White. 2001. "Automatic generation of truss model for optimal design of reinforced concrete structures." *Struct. J.* 98 (4): 431–442. https://doi.org/10.14359/10286.
Almeida, V. S., H. L. Simonetti, and L. O. Neto. 2013. "Comparative analysis of strut-and-tie models using smooth evolutionary structural optimization." *Eng. Struct.* 56 (Nov): 1665–1675. https://doi.org/10.1016/j.engstruct.2013.07.007.
Amir, O., and O. Sigmund. 2013. "Reinforcement layout design for concrete structures based on continuum damage and truss topology optimization." *Struct. Multidiscip. Optim.* 47 (2): 157–174. https://doi.org/10.1007/s00158-012-0817-1.
ASTM. 2016. *Standard specification for deformed and plain carbon-steel bars for concrete reinforcement*. ASTM A615-16. West Conshohocken, PA: ASTM.
Bontempi, F., and P. G. Malerba. 2001. "Stress path adapting strut-and-tie models in cracked and uncracked RC elements." *Struct. Eng. Mech.* 12 (6): 685–698. https://doi.org/10.12989/sem.2001.12.6.685.
Brown, M. D., and O. Bayrak. 2006. "Minimum transverse reinforcement for bottle-shaped struts." *ACI Struct. J.* 103 (6): 813. https://doi.org/10.14359/18233.
Bruggi, M. 2009. "Generating strut-and-tie patterns for reinforced concrete structures using topology optimization." *Comput. Struct.* 87 (23): 1483–1495. https://doi.org/10.1016/j.compstruc.2009.06.003.
Bruggi, M. 2016. "A numerical method to generate optimal load paths in plain and reinforced concrete structures." *Comput. Struct.* 170 (Jul): 26–36. https://doi.org/10.1016/j.compstruc.2016.03.012.
CEN (European Committee for Standardization). 2004. *Design of concrete structures*. Eurocode 2. Brussels, Belgium: CEN.
Chen, W., and D. Han. 2007. *Plasticity for structural engineers*. Plantation, FL: Ross Publishing.
Du, Z., W. Zhang, Y. Zhang, R. Xue, and X. Guo. 2019. "Structural topology optimization involving bi-modulus materials with asymmetric properties in tension and compression." *Comput. Mech.* 63 (2): 335–363. https://doi.org/10.1007/s00466-018-1597-2.
Duque, L. F. M., and B. Graybeal. 2017. "Fiber orientation distribution and tensile mechanical response in UHPFRC." *Mater. Struct.* 50 (1): 55. https://doi.org/10.1617/s11527-016-0914-5.
Gaynor, A. T., J. K. Guest, and C. D. Moen. 2013. "Reinforced concrete force visualization and design using bilinear truss-continuum topology optimization." *J. Struct. Eng.* 139 (4): 607–618. https://doi.org/10.1061/(ASCE)ST.1943-541X.0000692.
Guyon, Y. F. 1953. *Prestressed concrete*. London: Contractors Record and Municipal Engineering.
Herranz, U. P., H. S. María, S. Gutiérrez, and R. Riddell. 2012. "Optimal strut-and-tie models using full homogenization optimization method." *ACI Struct. J.* 109 (5): 605. https://doi.org/10.14359/51684038.
Higuchi, R., J. L. Jewett, and J. V. Carstensen. 2022. "Experimental investigation of ribbing pattern effect on the bonding qualities of water jet cut steel reinforcement." *Archit. Struct. Constr.* 2 (3): 455–463. https://doi.org/10.1007/s44150-022-00068-3.
Hsu, T. T. 1988. "Softened truss model theory for shear and torsion." *Struct. J.* 85 (6): 624–635. https://doi.org/10.14359/2740.
Jewett, J. L., and J. V. Carstensen. 2019. "Experimental investigation of strut-and-tie layouts in deep RC beams designed with hybrid bi-linear topology optimization." *Eng. Struct.* 197 (Oct): 109322. https://doi.org/10.1016/j.engstruct.2019.109322.
Klarbring, A., and N. Strömberg. 2013. "Topology optimization of hyperelastic bodies including non-zero prescribed displacements." *Struct. Multidiscip. Optim.* 47 (1): 37–48. https://doi.org/10.1007/s00158-012-0819-z.
Kwak, H.-G., and S.-H. Noh. 2006. "Determination of strut-and-tie models using evolutionary structural optimization." *Eng. Struct.* 28 (10): 1440–1449. https://doi.org/10.1016/j.engstruct.2006.01.013.
Leu, L.-J., C.-W. Huang, C.-S. Chen, and Y.-P. Liao. 2006. "Strut-and-tie design methodology for three-dimensional reinforced concrete structures." *J. Struct. Eng.* 132 (6): 929–938. https://doi.org/10.1061/(ASCE)0733-9445(2006)132:6(929).
Liang, Q. Q., B. Uy, and G. P. Steven. 2002. "Performance-based optimization for strut-tie modeling of structural concrete." *J. Struct. Eng.* 128 (6): 815–823. https://doi.org/10.1061/(ASCE)0733-9445(2002)128:6(815).
Liu, Y., J. L. Jewett, and J. V. Carstensen. 2020. "Experimental investigation of topology-optimized deep reinforced concrete beams with reduced concrete volume." In *Proc., RILEM Int. Conf. on Concrete and Digital Fabrication*, 601–611. Cham, Switzerland: Springer.
Sahoo, D. K., B. Singh, and P. Bhargava. 2011. "Minimum reinforcement for preventing splitting failure in bottle-shaped struts." *ACI Struct. J.* 108 (2): 206. https://doi.org/10.14359/51664256.
Sanders, E. D., A. Pereira, M. A. Aguiló, and G. H. Paulino. 2018. "PolyMat: An efficient Matlab code for multi-material topology optimization." *Struct. Multidiscip. Optim.* 58 (6): 2727–2759. https://doi.org/10.1007/s00158-018-2094-0.
Schlaich, J., K. Schäfer, and M. Jennewein. 1987. "Toward a consistent design of structural concrete." *PCI J.* 32 (3): 74–150. https://doi.org/10.15554/pcij.05011987.74.150.
Shao, Y., and S. L. Billington. 2022. "Impact of UHPC tensile behavior on steel reinforced UHPC flexural behavior." *J. Struct. Eng.* 148 (1): 04021244. https://doi.org/10.1061/(ASCE)ST.1943-541X.0003225.
Shao, Y., C.-C. Hung, and S. L. Billington. 2021. "Gradual crushing of steel reinforced HPFRCC beams: Experiments and simulations." *J. Struct. Eng.* 147 (8): 04021114. https://doi.org/10.1061/(ASCE)ST.1943-541X.0003080.
Shao, Y., and C. P. Ostertag. 2023. "LEGO-inspired and digitally-fabricated steel reinforcement cage for ultra-high performance concrete (UHPC) beams." *Eng. Struct.* 279 (Mar): 115617. https://doi.org/10.1016/j.engstruct.2023.115617.
Singh, B., A. Vimal, and G. Gaurav. 2018. "Whither transverse reinforcement in bottle-shaped struts?" *Structures* 14 (Jun): 43–55. https://doi.org/10.1016/j.istruc.2018.02.003.
Victoria, M., O. M. Querin, and P. Martí. 2011. "Generation of strut-and-tie models by topology design using different material properties in tension and compression." *Struct. Multidiscip. Optim.* 44 (2): 247–258. https://doi.org/10.1007/s00158-011-0633-z.
Williams, C., D. Deschenes, and O. Bayrak. 2012. *Strut-and-tie model design examples for bridges: Final report*. Austin, TX: Center for Transportation Research, Univ. of Texas.
Xia, Y., M. Langelaar, and M. A. Hendriks. 2020. "Automated optimization-based generation and quantitative evaluation of strut-and-tie models." *Comput. Struct.* 238 (Oct): 106297. https://doi.org/10.1016/j.compstruc.2020.106297.
Yang, R., and A. Chahande. 1995. "Automotive applications of topology optimization." *Struct. Optim.* 9 (3): 245–249. https://doi.org/10.1007/BF01743977.
Yuan, A., D. Xu, S. Qian, and H. Dai. 2018. "Splitting force of bottle-shaped struts with different height-to-width ratios." *Eng. Struct.* 167 (Jul): 481–493. https://doi.org/10.1016/j.engstruct.2018.04.048.
Zegard, T., and G. H. Paulino. 2013. "Truss layout optimization within a continuum." *Struct. Multidiscip. Optim.* 48 (1): 1–16. https://doi.org/10.1007/s00158-013-0895-8.
Zhang, X. S., G. H. Paulino, and A. S. Ramos. 2018. "Multi-material topology optimization with multiple volume constraints: A general approach applied to ground structures with material nonlinearity." *Struct. Multidiscip. Optim.* 57 (1): 161–182. https://doi.org/10.1007/s00158-017-1768-3.
Zhao, T., A. A. Alshannaq, D. W. Scott, and G. H. Paulino. 2023. "Strut-and-tie models using multi-material and multi-volume topology optimization: Load path approach." *ACI Struct. J.* 120 (6): 7. https://doi.org/10.14359/51739089.

Zhao, T., E. N. Lages, A. S. Ramos Jr., and G. H. Paulino. 2020. "Topology optimization considering the Drucker–Prager criterion with a surrogate nonlinear elastic constitutive model." *Struct. Multidiscip. Optim.* 62 (6): 3205–3227. https://doi.org/10.1007/s00158-020-02671-8.

Zhao, T., A. S. Ramos Jr., and G. H. Paulino. 2019. "Material nonlinear topology optimization considering the von Mises criterion through an asymptotic approach: Max strain energy and max load factor formulations." *Int. J. Numer. Methods Eng.* 118 (13): 804–828. https://doi.org/10.1002/nme.6038.

Zhiyi, Y., Z. Kemin, and Q. Shengfang. 2018. "Topology optimization of reinforced concrete structure using composite truss-like model." *J. Struct. Eng. Mech.* 67 (1): 79–85. https://doi.org/10.12989/sem.2018.67.1.079.

Zhou, L., Z. Liu, and Z. He. 2018. "Elastic-to-plastic strut-and-tie model for deep beams." *J. Bridge Eng.* 23 (4): 04018007. https://doi.org/10.1061/(ASCE)BE.1943-5592.0001206.

Zhu, J.-H., W.-H. Zhang, and L. Xia. 2016. "Topology optimization in aircraft and aerospace structures design." *Arch. Comput. Methods Eng.* 23 (4): 595–622. https://doi.org/10.1007/s11831-015-9151-2.